Supplementary Material for "Microstructure of Continuous Shear Thickening Colloidal Suspensions Determined by Rheo-VSANS and Rheo-USANS"

Yu-Fan Lee,[a] Yimin Luo,[a] Tianyi Bai,[a] Scott C. Brown,[b] and Norman J. Wagner[a]

[a] Center for Neutron Science, Department of Chemical and Biomolecular Engineering, University of Delaware, Newark, Delaware 19716
[b] The Chemours Company, Chemours Discovery Hub, Newark, Delaware 19713

S.1.   PEGylation of Silica Surface

PEGylation of silica surface was accomplished through silanization synthesis using the method of bulk deposition. This method assumes that sufficient amount of adsorbed moisture is present on the silica particles to cause silane hydrolysis. The silane of 2-[methoxy(polyethyleneoxy)6-9]propyltrimethoxysilane (with M_w =459-591 g/mol) was purchased from Gelest Inc. Silica particles were directly mixed with silane in a large grinder based on silane to silica weight ratio of 100:4. The mixture was ground thoroughly for 20 mins. After the grinding, the mixture was placed in a preheated vacuum oven overnight at 90 °C for curing. After heating overnight, the coated particles were washed with Milli-Q water and centrifuged to remove excess reactants, such as silane and silanol polymers. The washed suspension was again heated in a vacuum oven overnight at 90 °C. The resulting dry form of PEGylated silica particles was then collected.

Thermogravimetric analysis (TGA) and carbon analysis was performed to determine the amount of successful PEGylated coating on the silica. Thermogravimetric analysis for the dry form of silica nanoparticles was performed using Discovery TGA (TA Instruments, New Castle, DE) with a temperature ramp of 20 °C/min from room temperature to 800 °C. To correctly determine the weight fraction of the PEGylation coating, the extent of dehydration must be corrected for in the calculation, as bare silica and PEGylated silica adsorb different among of moisture. It has been reported that the dehydration occurs before 200 °C [1]. In this case the weight percentage was properly normalized by the sample weight at 200 °C for each measurement, as shown in Fig. S1. At the terminal temperature of the measurement, a 0.87 wt% difference was observed between bare and PEGylated silica, which confirms the successful coating of the PEGylation layer. Carbon analysis was performed on SC632 carbon determinator (LECO corporation) and calibrated with 1 wt% carbon reference standard. The results showed carbon composition of 0.065 wt% and 1.408 wt% for bare silica and PEGylated silica, respectively. Given the known weight percentage of carbon and the averaged surface area of silica particles, a grafting density of 4±1 PEG chains/nm^2 was obtained.
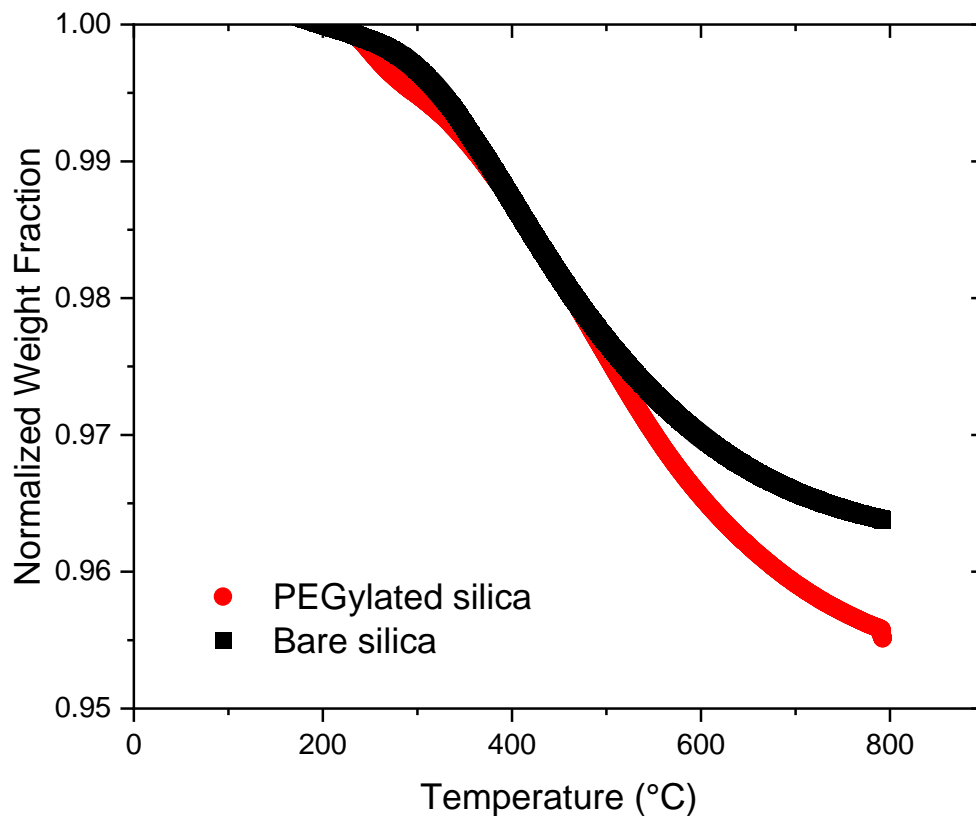
Figure S1:   TGA results for bare and PEGylated silica scanned at heating rate of 20 °C/min in dynamic air atmosphere. Weight fractions are normalized to the weight fraction measured at 200 °C.

S.2.   Transmission measurement

The measured transmission of Rheo-VSANS and Rheo-USANS for suspensions discussed in the main text is listed in Table SI and SII, respectively. The transmission does not vary substantially or systematically with shear flow for both suspensions, indicating the sample integrity is maintained during the Rheo-USANS and Rheo-VSANS experiments.

Table SI. Transmission measurement of PEGylated silica suspension in Rheo-VSANS.

PEGlyated SiO$_2$ suspension	
Shear Stress (Pa)	Transmission
1000	0.289
900	0.293
800	0.291
700	0.291

600	0.287
500	0.292
200	0.290
100	0.294
50	0.294
10	0.298
5	0.304
1	0.303
0	0.301

Table SII. Transmission measurement of bare and PEGylated silica suspension in Rheo-USANS.

	Shear Stress (Pa)	T_{wide}	T_{rock}	T_{rock}/T_{wide}
Bare SiO$_2$ suspension	0	0.720	0.675	0.938
	1000	0.719	0.675	0.938
	500	0.720	0.675	0.937
	50	0.720	0.685	0.952
	1	0.719	0.688	0.956
PEGlyated SiO$_2$ suspension	500	0.741	0.681	0.919
	0	0.742	0.688	0.927
	100	0.746	0.703	0.942
	20	0.747	0.694	0.929
	1	0.750	0.701	0.935
	1000	0.749	0.691	0.923

S.3. Estimated scattering intensity from confocal measurements in Cheng et al. [2]

Hydrocluster formation was visually identified with the aid of a combination of fast confocal microscopy with simultaneous rheological measurement in Cheng et al. [2] A threshold interparticle distance was defined for including a particle in a cluster and the probability, P_N, of obtaining a cluster with N particles was then determined. As it is understood that the scattering intensity of a cluster is volume-squared weighed to the cluster probability P_N, the estimated intensity thus can be written as:

$$\langle I \rangle \propto \int R^6 P_N dN \propto \int (N^{\frac{1}{D_f}})^6 P_N dN = \int N^{6/D_f} P_N dN , \qquad (S.1)$$

where R is the distance from the center of the cluster. We assume the internal structure of hydrocluster can be described by fractals with mass fractal dimension D_f,

$$N \propto R^{D_f}, \ 1 < D_f < 3 . \qquad (S.2)$$

Thus, the normalized scattering intensity can be estimated by dividing the scattering intensity under shear by the equilibrium scattering intensity

$$\frac{\langle I \rangle}{\langle I_0 \rangle} \sim \frac{\int N^{6/D_f} P_N dN}{\int N^{6/D_f} P_{N,Pe=0} dN} \,. \tag{S.3}$$

For stationary suspensions at Pe=0, an exponential distribution of clusters was reported for the equilibrium distribution, and this remained unchanged until Pe=3.6. To avoid errors from digitizing, an analytical exponential distribution was used for both Pe = 0 and 3.6, where the decay follows,

$$P_{N,Pe=0} = 5.129 \times e^{-1.72N} \,. \tag{S.4}$$

For the higher Pe results, numerical integrations were performed following Eq. (S.3). A fractal dimension of 2.5 was used for the calculation of the scattering intensity.

S.4. Rotational symmetry analysis for stress-SANS rule

In this section, we follow the symmetry analysis from Lee et al. [3] to calculate the parameters needed for stress-SANS rule analysis. In Lee et al.,[3] a more general method was developed to explore the structural symmetry of dense suspension during flow. This method is equivalent to the work of Gurnon and Wagner [4], where instead of performing integration over SANS data, nonlinear fitting with Fourier base function to the anisotropic scattering profile is achieved. Note that they presented the analysis on the 1-2 (velocity-velocity gradient) plane of shear, while the same analysis can also be performed on other planes of shear.

Here, we perform the same symmetry analysis on the 1-3 (velocity-vorticity) plane of shear. Before projecting to the 2D plane measurable from SANS, the scattering of suspension microstructures under flow can be described in terms of 3D spherical harmonic expansion with the spherical coordinate system shown:

$$S(\boldsymbol{q};Pe) = 1 + \sum_{l,m} B_{l,m}^+(q;Pe)(Y_{l,m}(\Omega_k) + (-1)^m Y_{l,-m}(\Omega_k)) \,. \tag{S.5}$$

The spherical harmonic coefficients $B_{l,m}^+(q;Pe)$ contribute to the stress contributions as elaborated in Gurnon and Wagner [4] and can be determined from the scattering measurements. After the projection of the 3D structure factor to the 1-3 shear plane, the structure factor can be recast in the Cartesian coordinate frame,

$$S^{gradient}(q,\theta) = 1 + B_{0,0}^+(q)\left(\frac{1}{\sqrt{\pi}}\right) - B_{2,0}^+(q)\left(\sqrt{\frac{5}{4\pi}}\right) + B_{2,2}^+(q)\sqrt{\frac{15}{8\pi}}\cos(2\theta) + B_{4,0}^+(q)\left(\frac{9}{8\sqrt{\pi}}\right)$$
$$+ B_{4,2}^+(q)\left(\frac{-3\sqrt{5}}{4\sqrt{2\pi}}\right)\cos(2\theta) + B_{4,4}^+(q)\left(\frac{3\sqrt{35}}{32\sqrt{2\pi}}\right)\cos(4\theta) \tag{S.6}$$

Note that θ represents the azimuthal angle as defined in the main text. To focus on the symmetric contribution to the structure factor, equation (S.5) is rearranged via Fourier series expansion with

orthogonal base functions as shown below, where coefficients are assigned for each sinusoidal base function,

$$S^{gradient}(q,\theta,\dot{\gamma}) = c_0 + \sum_{n=1}^{\infty} c_{2n-1} \sin(2n\theta) + c_{2n} \cos(2n\theta), c_n = c_n(q,\dot{\gamma})$$

$$= c_0 + c_1 \sin 2\theta + c_2 \cos 2\theta + c_3 \sin 4\theta + c_4 \cos 4\theta + ... \tag{S.7}$$

$$c_0 = 1 + B_{0,0,q-avg}^+ \left(\frac{1}{\sqrt{\pi}}\right) - B_{2,0,q-avg}^+ \left(\sqrt{\frac{5}{4\pi}}\right) + B_{4,0,q-avg}^+ \left(\frac{9}{8\sqrt{\pi}}\right), \tag{S.8}$$

$$c_2 = B_{2,2,q-avg}^+ \left(\sqrt{\frac{15}{8\pi}}\right) + B_{4,2,q-avg}^+ \left(\frac{-3\sqrt{5}}{4\sqrt{2\pi}}\right), \tag{S.9}$$

$$c_4 = B_{4,4,q-avg}^+ \left(\frac{3\sqrt{35}}{32\sqrt{2\pi}}\right). \tag{S.10}$$

It is understood that the hydrodynamic stress includes $B_{0,0}^+, B_{2,0}^+, B_{2,2}^+, B_{4,0}^+$ and $B_{4,2}^+$ terms from spherical harmonic expansion analysis of the microstructure. Equation (S.8) is the equation that includes the most of spherical harmonic terms for hydrodynamic stress in the plane measured during Rheo-VSANS. Therefore, we chose c_0 to define the hydrodynamic stress contribution for stress-SANS analysis as described in Equation (6) from the main text. Note that as the anisotropic microstructure only occur at the low q, a q-range has been selected for performed the annular average described in the main text. $S_{q-avg}^{gradient}(\theta,\dot{\gamma})$ represents the data reduced from annular average at the q-range chosen, and once obtained, statistical fitting can be performed to extract the coefficients defined in (S.7). As the high-resolution 2D form of the structure factor is not available due to multiple scattering and instrument smearing, the symmetry analysis was performed on the scattering intensity by assuming,

$$\frac{I_{q-avg}^{gradient}(\theta,\dot{\gamma})}{I_{q-avg}^{gradient}(\theta,\dot{\gamma}=0)} \cong \frac{S_{q-avg}^{gradient}(\theta,\dot{\gamma})}{S_{q-avg}^{gradient}(\theta,\dot{\gamma}=0)}. \tag{S.11}$$

Then, the structure factor associated with its Fourier expansion can be written in a dimensionless form as presented in the main text,

$$S_{q-avg}^{gradient*}(\theta,\dot{\gamma}) = \frac{S_{q-avg}^{gradient}(\theta,\dot{\gamma})}{S_{q-avg}^{gradient}(\theta,\dot{\gamma}=0)} = c_0^* + c_2^* \cos 2\theta + c_4^* \cos 4\theta. \tag{S.12}$$

S.4. Peakhold measurements of the bare and PEGylated silica suspension

In Figure S.2 are shown the results of 30-min stress peakhold measurements around the shear thickened state for the bare and the PEGylated silica suspension studied in the main text. The constant viscosity seen in panels (a) and (c) is expected for suspensions that exhibit steady reversible continuous shear thickening. Significant fluctuations in N_1 at high shear stresses reported in panels (b) and (d) agree with published results for similar suspensions in the strongly shear thickening regime [3,5,6]. In general, even with notable fluctuations, our time resolved N_1 measurements show largely negative values for both suspensions studied, except that a temporal broad positive peak is observed for the bare silica suspension at the highest applied stress of 2000 Pa. The fluctuations have generally been attributed to the dilation effect [7,8], and the formation of transient hydroclusters [9] or frictional networks [10], which break and reform in the shear thickened state. These three phenomena could also contribute to the broad positive peak observed for the bare silica suspension. However, connecting the dilation effect and the stress fluctuations requires further careful observation of the air-suspension interfaces [11]. Distinguishing the origin of the stress fluctuations between the dilation or transient hydroclusters formation/frictional networks remains challenging for future investigation.
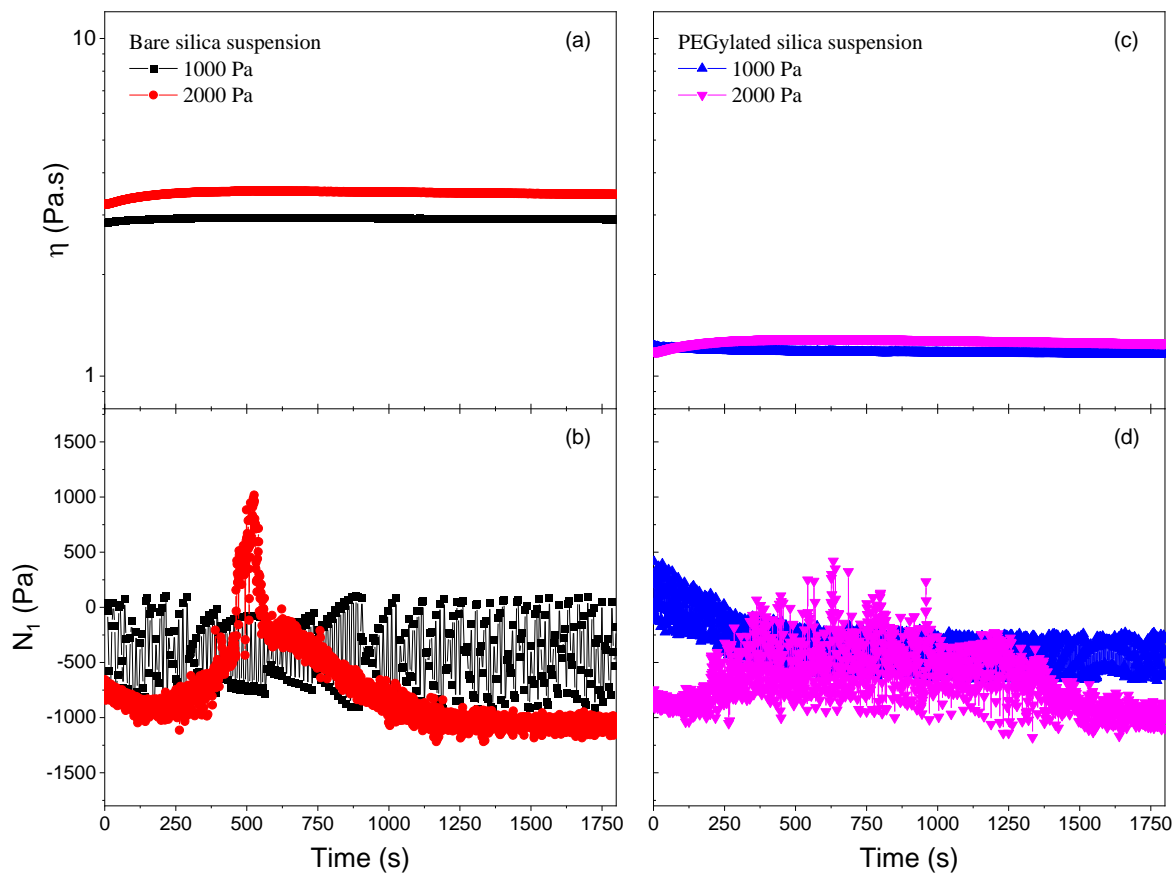
Figure S.2: Time-dependent measurements of viscosity and first normal stress difference at selected peakhold shear stresses (corresponding to the star symbols in Fig. 2 in the main text) for (a, b) bare silica suspension, and (c, d) PEGylated silica suspension with a sampling time of 1 s per data point.

References

[1]   J. M. Kim, S. M. Chang, S. M. Kong, K.-S. Kim, J. Kim, and W.-S. Kim, Ceramics International **35**, 1015 (2009).
[2]   X. Cheng, J. H. McCoy, J. N. Israelachvili, and I. Cohen, Science **333**, 1276 (2011).
[3]   Y.-F. Lee, Y. Luo, T. Bai, C. Velez, S. C. Brown, and N. J. Wagner, Physics of Fluids **33**, 033316 (2021).
[4]   A. K. Gurnon and N. J. Wagner, Journal of Fluid Mechanics **769**, 242 (2015).
[5]   J. R. Royer, D. L. Blair, and S. D. Hudson, Phys Rev Lett **116**, 188301 (2016).
[6]   D. Lootens, H. van Damme, Y. Hemar, and P. Hebraud, Phys Rev Lett **95**, 268302 (2005).
[7]   E. Brown and H. M. Jaeger, Journal of Rheology **56**, 875 (2012).
[8]   E. Brown and H. M. Jaeger, Rep Prog Phys **77**, 046602 (2014).
[9]   D. R. Foss and J. F. Brady, Journal of Fluid Mechanics **407**, 167 (2000).
[10]   R. Mari, R. Seto, J. F. Morris, and M. M. Denn, Journal of Rheology **58**, 1693 (2014).
[11]   R. Maharjan, E. O'Reilly, T. Postiglione, N. Klimenko, and E. Brown, Phys. Rev. E **103**, 012603 (2021).